Aerodynamic State Estimation of a Bio-Inspired Distributed Sensing UAV at High Angles of Attack and Sideslip

Timothy Ward[1,†], Sourish Mukherjee[2,†], Shane P. Windsor[1] and Sergio A. Araujo-Estrada[2]

***Abstract*— Biological fliers' remarkable manoeuvrability and robust flight control are aided by information from dense arrays of distributed flow sensors on their wings. Bio-inspired fixed-wing uncrewed aerial vehicles (UAVs) with a "flight-by-feel" control approach could mimic these abilities, allowing safe operation in cluttered urban areas. Existing work has focused on longitudinal parameter estimation and control at low angles of attack. This wind-tunnel study estimates both the longitudinal and lateral-directional aerodynamic states of a bio-inspired distributed pressure sensing UAV at angles of attack and sideslip up to 25° and 45°. Four span-wise strips of pressure sensors were found to show strong, location dependent variation with angle of sideslip across all angles of attack, indicating that distributed pressure sensing arrays can encode lateral-directional flow information. This was supported by the use of the pressure signals in estimator algorithms, which showed angle of sideslip estimation was possible with both a linear partial-least-squares regression-based estimator and a non-linear feed-forward artificial neural network estimator. The non-linear estimator could predict angle of sideslip with a lower error than the linear estimator, with a root-mean-square error (RMSE) of 0.70° for the former compared to 1.23° for the latter. They both showed good estimation of angle of attack, even in the post-stall regime, with an RMSE of 0.58° for the linear estimator and 0.54° for the non-linear estimator. These results show that pressure-based distributed sensing can capture a complete aerodynamic picture of a UAV, unlocking the potential of a "flight-by-feel" control system informed by the aerodynamic states of the vehicle across a wide range of aerodynamic conditions.**

I. INTRODUCTION

Applications of fixed-wing uncrewed aerial vehicles (UAVs) such as ecological monitoring and last-mile cargo delivery require long-range, low-level flight [1]. This is a challenging flight regime which requires high manoeuvrability [2], both to navigate cluttered urban environments and to cope with gusty, turbulent conditions caused by the proximity to terrain [3]. Control challenges are heightened due to the large proportion of the turbulence in these environments that has a length scale similar to that of a small fixed-wing UAV, causing contrary flow disturbances on either wing which lead to lateral-directional perturbations in roll and yaw [4].

Conventional UAVs use an inertial measurement unit and magnetometer to measure the acceleration, rotational rate, and orientation of the UAV's centre of mass [5], which is typically referenced against supplemental airspeed and position data from a pitot-static tube and a global navigation satellite system (GNSS) receiver [6]. This sensing architecture enables autonomous flight control when coupled with a flight dynamics and aerodynamics model of the associated UAV. However, control effectiveness is limited by the lack of aerodynamic state (angle of attack, α, and angle of sideslip, β) information, which usually forces the model to assume linear aerodynamics (low α and β) [7]. This limits the flight envelope of the UAV, generally preventing autonomous dynamic manoeuvres that exploit non-linear aerodynamics, such as sharp heading changes [8]. The lack of local aerodynamic state information also impedes the response to local flow perturbations caused by turbulent conditions; the control system can only respond to the bulk disturbance of the UAV's centre of mass [4]. Coupled with a small UAV's low inertia, this results in poor trajectory control in many fixed-wing UAVs, limiting their use in space-restricted environments [9].

In contrast, biological fliers such as insects, birds and bats exhibit precise control and high manoeuvrability, while flying in similarly challenging environments [10]. They employ a "sensor-rich" [11] control architecture which features many flow sensors distributed around their bodies. Bats' wings are covered in flow-sensitive hairs [12], hypothesised to act as airflow direction indicators, providing warnings of flow separation and stall during sharp manoeuvres [12]. Similarly, birds have thousands of Herbst corpuscles distributed on their wings and body [13] which have been shown to be sensitive to changes in airflow [14]. They are highly sensitive to specific vibration ranges [13], which is thought to allow detection of flow separation [14], contributing to the detection of high angle of attack and stall.

Biological sensing has inspired a growing field of "flight-by-feel" [15] research, which aims to equip UAVs with distributed sensing systems to provide local flow information. This could allow UAVs to exploit a larger, non-linear flight envelope, by allowing the detection of local flow separation and stall [16]; it could allow for more rapid detection of and response to gusts [17]; and it could produce UAVs that are robust to sensor dropout and damage [18].

The literature to date has made use of many distributed sensor types, including artificial hair sensors [19], strain sensors [20], and a variety of pressure sensor types [21]–[23]. The data generated by these sensor networks can then be used towards flight control in different ways. Early work by Yeo et al. [22] discretised the tailplane of a UAV into sections centred around a differential pressure sensor, then

† Authors contributed equally.

[1]Timothy Ward and Shane P. Windsor are with the Department of Aerospace Engineering, University of Bristol, Bristol, United Kingdom. timothy.ward@bristol.ac.uk, shane.windsor@bristol.ac.uk

[2]Sourish Mukherjee and Sergio A. Araujo-Estrada are with the Department of Aeronautical and Astronautical Engineering, University of Southampton, Southampton, United Kingdom. sourish.mukherjee@soton.ac.uk, s.araujo-estrada@soton.ac.uk

directly calculated the resulting aerodynamic loads. A more common approach is to use the distributed data to estimate aerodynamic states and loads, through both linear and non-linear means [19], [20]. These estimates can then be used in control, such as the pitch control based on α estimation achieved by Wood et al. [18]. An alternative control strategy is to input the distributed data into artificial neural network based end-to-end flight controllers. Haughn et al. [24] used this technique to effectively reduce the impact of generated gusts in a pitching aerofoil experiment, while Guerra-Langan et al. [25] used reinforcement learning to control the lift coefficient of a single degree of freedom wind tunnel model.

The present work uses distributed pressure sensors for aerodynamic state estimation. There is some evidence that distributed pressure sensors encode more flow information than other sensor types, such as strain sensors. It has been found that pressure sensors alone can give an almost as accurate angle of attack prediction as a combination of pressure and strain sensors, and can be an order of magnitude more accurate than strain sensors alone [20]. It has also been found that distributed pressure sensors could act as a local stall warning mechanism [2], an ability that has not been demonstrated using strain sensors.

Most of the existing literature has focused solely on the estimation or control of longitudinal parameters (such as pitch, lift, drag, and α). Additionally, very little work has attempted to estimate aerodynamic states under non-linear conditions. Li et al. [21] calibrated an iterative robust regression model to estimate both α and β, but only considered maximum angles of $\alpha = 15^\circ$ and $\beta = 10^\circ$. Araujo-Estrada & Windsor [20] estimated α successfully between $-15^\circ < \alpha < 20^\circ$, and noted that the root-mean-square-error (RMSE) between actual and estimated α increased substantially above $\alpha = 10^\circ$. No work has yet estimated angle of sideslip beyond 10° using flow sensor arrays. The ability to estimate β, as well as lateral loads, could be crucial to allow a full distributed-sensing based flight controller to exploit advantages such as an expanded flight envelope. Levin et al. [8] recorded sideslip angles up to $\beta = \pm 30^\circ$ during a pre-programmed space-minimised 180° heading change - such a manoeuvre would be a useful obstacle avoidance ability for safe UAV flight in congested areas.

To this end, this work investigates whether a UAV with bio-inspired distributed pressure sensors across its wings (Fig. 1) can estimate its aerodynamic angles (α and β) across a wide spectrum of linear and non-linear flight conditions, up to $\alpha = 25^\circ, \beta = 45^\circ$. The results of both a partial-least-squares (PLS) based linear estimator and an artificial neural network (ANN) estimator are presented.

The rest of this paper is organised as follows. Section II introduces the experimental and data analysis methods employed. Section III displays the impact of high angles of sideslip and attack on recorded distributed pressure sensor and force balance readings, while Section IV presents the aerodynamic state estimation process and results. Section V discusses the significance of the findings and suggests future related work. Finally, Section VI summarises the work.

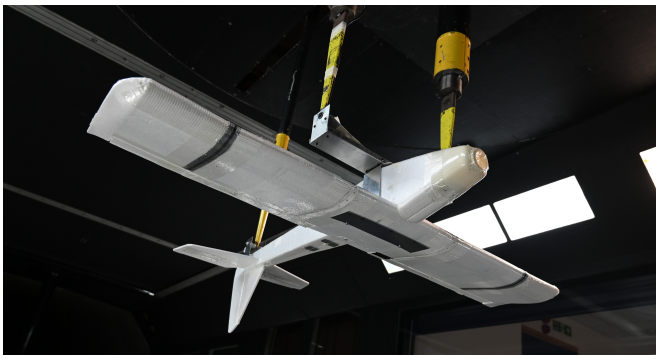

Fig. 1: UAV mounted to wind tunnel overhead balance.

II. METHODS

A. Bio-Inspired Distributed Sensing UAV

The featured bio-inspired distributed sensing UAV is a modified foam-based model aircraft - the Ripmax WOT4 Foam-E Mk2+. The wing has a rectangular planform of chord length $c = 0.25m$ and span $b = 1.205m$. The propeller, motor and landing gear were removed for these wind tunnel tests, but the rest of the fuselage and the empennage were left unmodified, with functional control surfaces. The aircraft was mounted upside down to the wind tunnel struts with a bracket that replaced the landing gear. Bolts also clamped the bracket to the wing, to reduce vibrations. The configuration mounted in the wind tunnel is shown in Fig. 1.

The UAV features a bespoke aerofoil with a measured $t/c = 18.5\%$. A semi-span wing with the same aerofoil was experimentally characterised in previous work [20]. The aerofoil was thick enough to allow simple integration of the distributed pressure sensing array into the wing, which comprised of four 3D-printed chord-wise strips of pressure ports bonded to an aluminium spar inserted into the foam. Fig. 2a shows the planform of the wing, highlighting the location of these pressure-sensing strips.

Each inboard strip was instrumented with seven pressure sensors, while each outboard strip was populated with eight sensors. The pressure ports were in the same locations for each wing, and were chosen based on prior experiments with the semi-span wing [20], from which an indication of the most information-rich pressure port locations had been gathered. The chord-wise distribution of pressure sensors around the aerofoil is shown in Figs. 2b and 2c. Only the sensors that successfully recorded data in at least one strip are shown; a total of four sensors failed. The total number of usable sensors was therefore 26.

Analogue differential pressure sensors (Sensirion SDP36) were chosen to record pressure data, at 200Hz. They were attached to custom PCBs inside the wing. The analogue signals were digitised and processed by a micro-controller unit (MCU) in each wing, before a fuselage-mounted MCU synchronised and communicated these to the control PC over Universal Serial Bus (USB). A summary of the instrumentation and data acquisition configuration is shown in Fig. 2a.

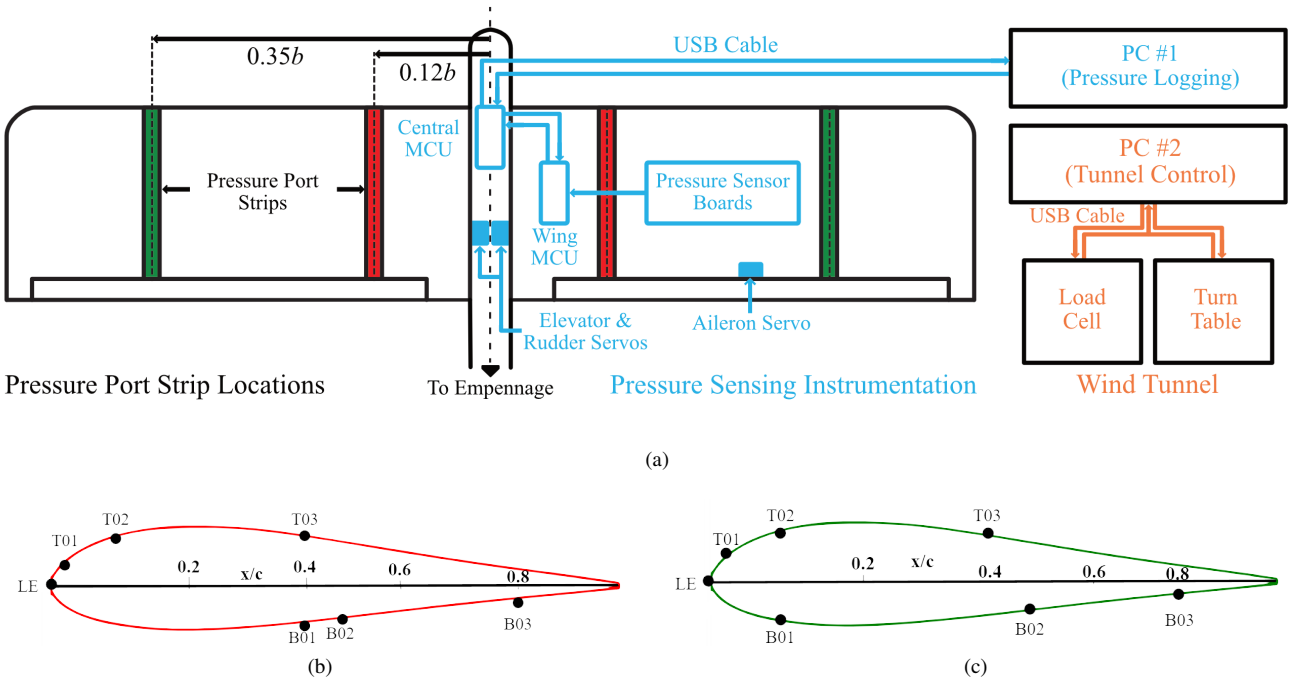

Fig. 2: Pressure sensing configuration: **(a)** span-wise pressure port strip locations and instrumentation, **(b)** inboard strip chord-wise sensor placements (red, N.B. sensor B01 did not record for the right wing), and **(c)** outboard strip chord-wise sensor placements (green, N.B. sensor B03 did not record for the right wing).

B. Wind Tunnel Testing Apparatus and Methodology

The R.J. Mitchell Wind Tunnel at the University of Southampton was used for the tests. The tunnel features a working section of $3.5m$ by $2.4m$, with a turbulence intensity of 0.2%. The UAV was attached to a 6-component overhead balance, set into a turntable allowing for yaw and pitch movements. Before testing, a laser inclinometer was used to equate the tunnel's pitch angle with the UAV's angle of attack, and the overhead balance was calibrated. During testing, an automated script was used to move between each experimental angle set-point at each wind-speed ($10m/s, 14m/s, 16m/s$). The UAV was taken to each set-point, paused for 5 seconds, then held still while a 15-second time history of loads and pressure data was collected at each point. An experimental test matrix detailing the chosen test angle combinations is shown in Fig. 3. The density of α readings was reduced for $-4° < \alpha < 10°$, as data from previous work [20] suggested that this region was expected to follow a predictable linear lift-curve slope. This work focuses on the effects of high aerodynamic angles, so a dense dataset in these regions was prioritised given wind tunnel time constraints. The reduced range of angles tested for the $16m/s$ wind-speed (due to wing loading concerns) is highlighted, along with the extremes of the estimator training datasets (see Section IV).

C. Loads Data Calibration & Corrections

The wind tunnel loads data were measured using the wind tunnel reference frame point (1300mm from the tunnel ceiling). This meant that the moments were measured in the wind-axis frame, which in turn included virtual moments from the forces. Different orientations led to a shift in the location of the centre of gravity (CG) with respect to the reference point. To account for this shift, the moments were recorded with no wind across various angles. From these data points, an equation of a plane was approximated using least squares regression. The selected plane was sinusoidal since the position of CG varied like a simple harmonic pendulum. This plane was then used to remove the contribution of weight on the moments measured during wind tunnel testing. Refer to Appendix A for more details.

The forces acting on the balance and struts were also accounted for when correcting the loads data. The forces were measured by collecting loads data for just the struts at the three different wind speeds, with varying α and β. The pitching moment coefficient of the struts was calculated by using the wing's area, to allow for equal comparison with the raw data. A sinusoidal plane was generated, due to the struts' circular motion with varying orientations. The reference point was shifted from the wind tunnel reference point to the quarter mean aerodynamic chord of the UAV to verify the pitching moment from the tail. Similar procedures were undertaken for rolling and yawing moments. The measured forces were then corrected by removing the struts' force contributions. Finally, the forces were rotated, since the forces were measured with respect to the balance turntable's rotation rather than the wind direction.

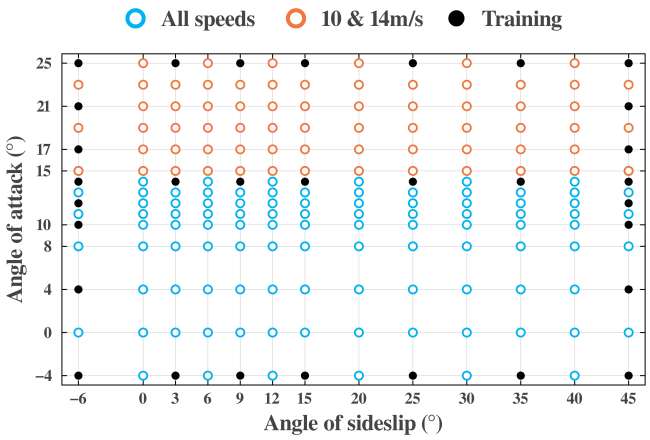

Fig. 3: Experimental test matrix showing the angle combinations chosen for testing, for all speeds (blue) and for all except $16m/s$ (orange). Filled points were manually selected to be part of the estimators' training dataset (see Section IV).

D. Pressure Signals Processing

Time histories of each pressure sensor were recorded at each experimental condition; many of these were found to contain a number of large outlier values. No dominant frequencies were found in the time histories that could have suggested an aerodynamic explanation, such as vortex shedding. However, it was noted that anomalies of similar magnitudes occurred across sensors on opposite sides of the sensing array within the same sample time, before an aerodynamic effect could have propagated. The outliers were therefore most likely electrical in nature, and were removed if they were further than three median absolute values from the median. This is a robust statistic to use for anomaly removal, as it is insensitive to outliers [26]. After this process, which removed a mean of 15.9% of the data points collected from each time history, the pressure sensor time histories fit a Gaussian distribution. Median, mean, and standard deviation values were then obtained for each sensor at each condition, and normalised into coefficients of pressure, C_p, as follows:

$$C_{p_i} = \frac{p_i - p_\infty}{q_\infty} \tag{1}$$

Where p_∞ and q_∞ represent the freestream static pressure and dynamic pressure respectively. The C_p values were corrected with a small offset, obtained by calculating the maximum of a 2nd order polynomial fitted to the C_p values from the leading edge pressure port of each sensor strip at $\beta = 0°, \alpha = (-4°, 0°, 4°, 8°)$. The maximum of this polynomial represents the stagnation point experienced by the leading edge of a cambered aerofoil at a low negative angle of attack. By definition, the coefficient of pressure at the stagnation point is equal to unity (as $q_\infty = p - p_\infty$); so the difference, if any, between the maximum of this polynomial and unity can be used to correct the coefficients of pressure. This procedure was performed separately for each sensor strip, with a mean correction of just 0.1 - likely explainable by the level of accuracy of the freestream static pressure measurement.

III. Results for High Aerodynamic Angles

High angles of sideslip lead to considerable changes in aerodynamic loads and the received pressure signals, as demonstrated in Fig. 4. The lift and drag of the UAV at different angles of attack (at $\beta = 0°$) are characterised in Fig. 4a. The gentle stall is noteworthy and seems to be a characteristic feature of the wing section, likely exacerbated by the relatively low Reynolds number. The lateral-directional loads are shown in Fig. 4b. The rolling and yawing moments exhibited a linear correlation between the angle of sideslip and the moment coefficients. The side force increases linearly with β, but decreases non-linearly over the post-stall α range. This agrees with previous observations [27], and is likely due to stall-induced boundary layer separation.

The pressure sensing data shows considerable variation with increasing α and β. Fig. 4c shows the pressure signal of the leading edge sensor in each span-wise strip against angle of attack, for $\beta = 0°$. A linear relationship is observed between $4° \leq \alpha \leq 10°$; above this, individual pressure sensors diverge considerably through the stall. Fig. 4d shows the response of the same leading edge pressure signals to the angle of sideslip, at $\alpha = 8°$. All of the leading edge sensors show broadly linear variation with sideslip angle; however, the inboard sensors experience a much more significant change than the outboard sensors. The left wing sensors, which were pointing upstream at high angles of sideslip, experience a decrease in coefficient of pressure with increasing sideslip, while the right wing sensors - pointing downstream and at least partly shielded by the fuselage - experienced an increase in coefficient of pressure, correlating to a lower relative flow velocity. These observations demonstrate how much information can be encoded by even a few pressure sensors. These observations were coherent across all speeds measured, where the coefficients of forces and pressures had only small variations because of the low variations in Reynolds number.

IV. Aerodynamic State Estimation

As discussed in Section III, pressure signals respond in an almost linear manner to increasing angle of attack before stall occurs. For this reason, previous work in [20] used a linear estimator to predict angle of attack response. It was found to perform well until stall, beyond which the error increased. The work in [20] also employed an artificial neural network (ANN) as a type of non-linear estimator, and found that this could predict angle of attack well, even after stall. A robust iterative regression non-linear estimator as used in [21] was also found to predict low angles of attack and sideslip well. It was decided for the present work to compare the performance of both a linear and non-linear estimator across the entire range of angles of attack and sideslip, as the impact of estimator choice on higher sideslip angles had not been previously shown.

A. Partial Least Squares Linear Estimator

The chosen linear estimator was based on partial least squares (PLS) regression. This technique was chosen because

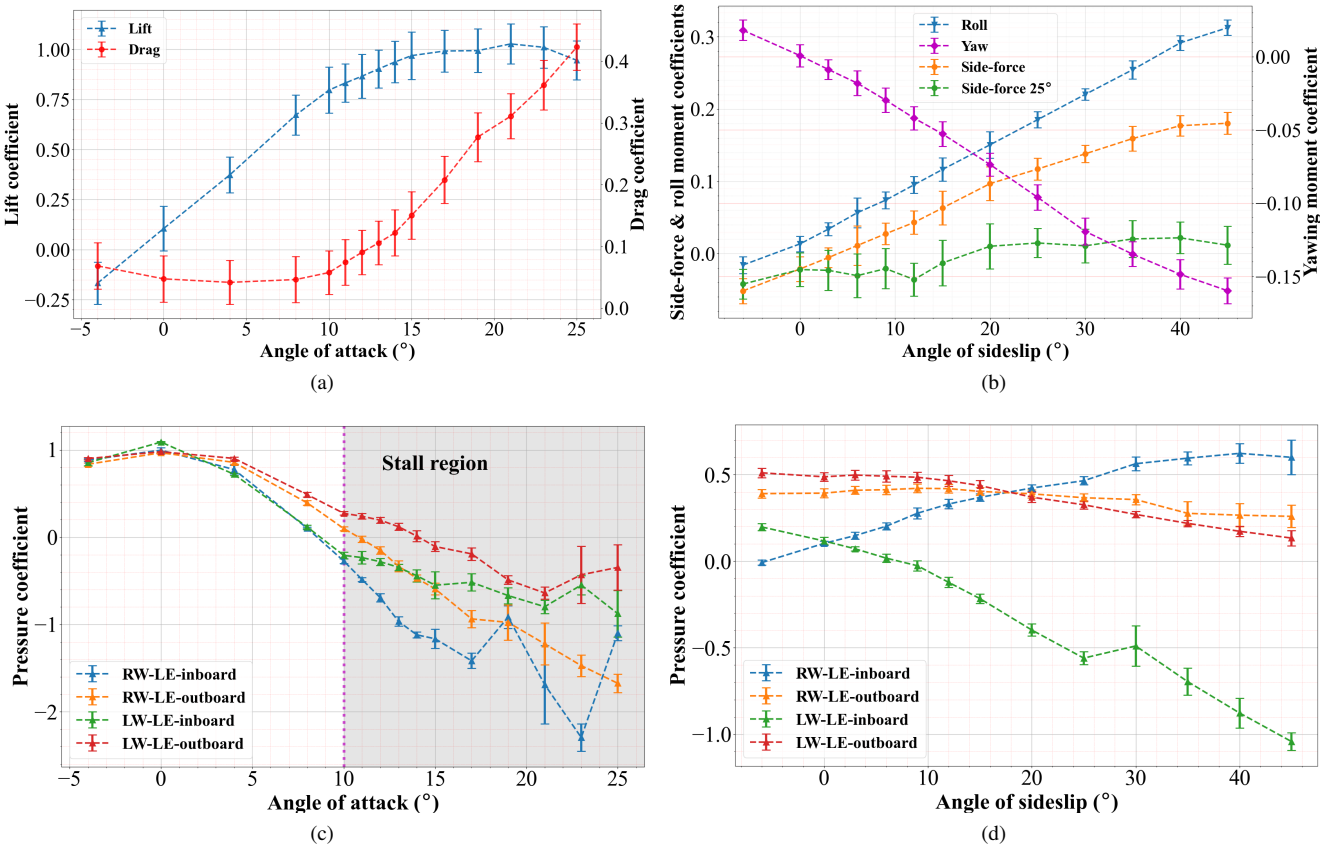

Fig. 4: Loads & pressure measurements at 14m/s: **(a)** longitudinal forces at $\beta = 0°$, **(b)** lateral-directional loads at $\alpha = 8°$ (and side-force at $\alpha = 25°$), **(c)** longitudinal leading edge pressures variation at $\beta = 0°$ and **(d)** lateral leading edge pressures variation at $\alpha = 8°$. Error bars represent a single standard deviation from the mean values plotted.

it is well suited for regression problems with a large number of correlated predictors of the response variables (such as a set of pressure signals responding to aerodynamic states). It finds the linear combinations of predictors (known as components) that are most covariant with the response variable (i.e., the predictors most sensitive to changes in the response) [28]. The output of the regression is a vector of weights, B, which can be multiplied by the matrix of predictors, X, to produce an estimation of the response variables, $\hat{Y}$ as follows:

$$\hat{Y} = XB \tag{2}$$

To produce the final aerodynamic angles estimator, PLS regression was performed (using the *plsregress* function in MATLAB Release 2024b) separately for training data collected at each speed, to obtain three weights vectors. To estimate an aerodynamic angle, the speed is used to lookup the correct weights vector, before (2) is used to obtain the estimate. Most UAVs are equipped with a pitot-static tube, so reliance on airspeed for the estimation is not impractical. However, it is also possible to predict airspeed with distributed pressure sensing data, as shown in [20], meaning angle estimation would still be possible with pressure sensing alone.

PLS regression calculates a specified number of components to perform the regression. For this work, 16 PLS components were chosen, as this value was sufficient to explain 99.7% of the variance in the data at each speed, and was still quick to compute. A convergence study was then performed to determine what ratio of the available data should be used for training as opposed to testing. The study was carried out by training the estimator with between 15% and 100% of the available data. Each training dataset was selected by first ensuring the extremes of the wind tunnel test matrix were captured (selected values are highlighted in Fig. 3) before randomly selecting further points from the remaining data. The extreme values were selected for training due to an expectation of complex behaviour at the highest angles, and to prevent the estimators from having to extrapolate a relationship over an angle range they weren't trained on. It was found that, for the PLS-based estimator, RMSE convergence occurred for α estimation with only 30% of the dataset used for training (and 70% for testing). Estimation of β required a 50% training to 50% testing split to converge. However, for the final results a 70% training to 30% testing split was used to estimate both angles, to ensure fair comparison with the non-linear estimator which required this increased level of training data.

B. Artificial Neural Network Nonlinear Estimator

A feed-forward artificial neural network (ANN) was chosen as the non-linear estimator, as this technique had shown good estimation results for both distributed hair sensors [19] and pressure sensors [20], [23]. The structure of an ANN consists of layers of interconnected artificial neurons, with each neuron placing a non-linear activation function over a linear mapping of its inputs. Feed-forward ANNs are universal approximators, mapping complex relations between input features and outputs [29], such as the relationship between pressure signals and aerodynamic angles.

ANN estimators have tunable hyperparameters, including the number of neurons per layer, the number of hidden layers, and the activation function of each neuron. The estimator for this work was selected by exploring the estimation performances of many ANNs tuned from a known baseline. The successful estimators used in [20] served as the starting point, then the number of layers in the network, the layer width and the neurons' activation function were methodically changed until a small network with reasonable performance was found. The selected ANN featured an input layer of 26 neurons (one per functional sensor reading), 3 hidden layers in a $(25, 15, 9)$ configuration, and an output layer with one neuron per estimated angle. It used the ReLU (rectified linear unit) activation function for all layers.

The loss function used to train the model was the mean-squared-error (MSE) between the actual and predicted angles. The model was implemented and trained with the *fitrnet* function in MATLAB Release 2024b, which uses the limited-memory Broyden-Fletcher-Goldfarb-Shanno (LBFGS) algorithm [30] to minimise the loss function. The training to testing data ratio used was the same 70% to 30% split that was used for the PLS-based estimator; an identical dataset of observation points was used to ensure fair comparison.

The chosen ANN was selected to balance network size and relative accuracy; a more thorough investigation of ANN architectures was out of scope for this work. To ensure this relative accuracy had been achieved, a large number of ANN sizes were trialled by using a Bayesian optimisation algorithm (built-in to *fitrnet*) for hyperparameter tuning. This process explored a wide range of ANN sizes, but only resulted in minor estimation improvements ($\approx 0.1^\circ$ RMSE) over the chosen model, at the expense of a much larger network (in the region of hundreds of neurons). Therefore, the chosen network represents a sensible compromise between network size and estimation performance. Future work could investigate different ANN architectures and training techniques, either to maximise estimation accuracy or for use in real-time force estimations, as demonstrated in [31].

C. Estimator Results & Error Analysis

The final RMSE values between estimated and actual responses are presented in Table 1. Both estimators provide similar results for α estimation (RMSE $\approx 0.55^\circ$). In contrast, the non-linear ANN estimator outperforms the linear estimator for β estimation, with almost half the RMSE value. However, the PLS-based estimator's overall level of error is still small in comparison to the range of sideslips tested, and could be suitably accurate for use in a control system.

A comparison of the α and β estimators' error distributions across all angle combinations, shown in Fig. 5, provides more insight into the results. Estimation errors in α (Fig. 5a and Fig. 5b) were consistently small for the PLS-based estimator, across the ranges of α and β. By contrast, the ANN estimator had a relatively high spread of α errors in the region $-6^\circ \leq \alpha \leq 8^\circ$ (RMSE $= 0.82^\circ$ compared to the linear estimator's RMSE $= 0.52^\circ$), but outperformed the linear estimator in the range $\alpha \geq 10^\circ$, with RMSE $= 0.33^\circ$ compared to 0.61°. The possible causes of this result are discussed in Section V. The ANN also showed reducing α estimation accuracy with increasing β, unlike the PLS-based estimator.

The β estimation errors (Fig. 5c and Fig. 5d) were much more consistent across the full range of both α and β; neither estimator had a significantly higher spread in any region. The ANN outperformed the PLS-based estimator, with a smaller error distribution corresponding to the much lower RMSE. The annotations in Fig. 5 represent the test points with the largest magnitude α estimation error (Figs. 5a and 5b) and β estimation error (Figs. 5c and 5d), for each estimator type; these are discussed in Section V.

V. DISCUSSION

Bio-inspired distributed pressure sensing has been successfully used for longitudinal state estimation and control [18], [20], but little work on lateral control has been performed. This work has investigated the potential for pressure-based lateral state estimation and control - even in the complex post-stall, high sideslip aerodynamic regime - through wind tunnel tests of a UAV with a bio-inspired pressure sensing array distributed across several span-wise locations.

The wind tunnel tests have shown that the UAV experiences significant increases in yawing and rolling moments with increasing sideslip angle, and simultaneous strong variation in pressure signals. It is already known that distributed pressure signals can contain information about complex longitudinal behaviours, such as hysteresis during dynamic pitching [20]. This work suggests that a large amount of lateral flow-state information is also encoded into the pressure signals from distributed arrays.

Further evidence of this can be seen in the distinct responses that pressure signals at different span-wise locations have to the same angles of sideslip. As shown in Fig. 4d, the inboard sensors have stronger reactions to β than the outboard sensors, highlighting flow effects such as fuselage-wing interaction at high angles of sideslip. The importance of span-wise distributed sensors was also discussed by Groves-

TABLE I: Estimator RMSE Results.

	α **RMSE** ($^\circ$)	β **RMSE** ($^\circ$)
PLS	0.580	1.228
ANN	0.542	0.700

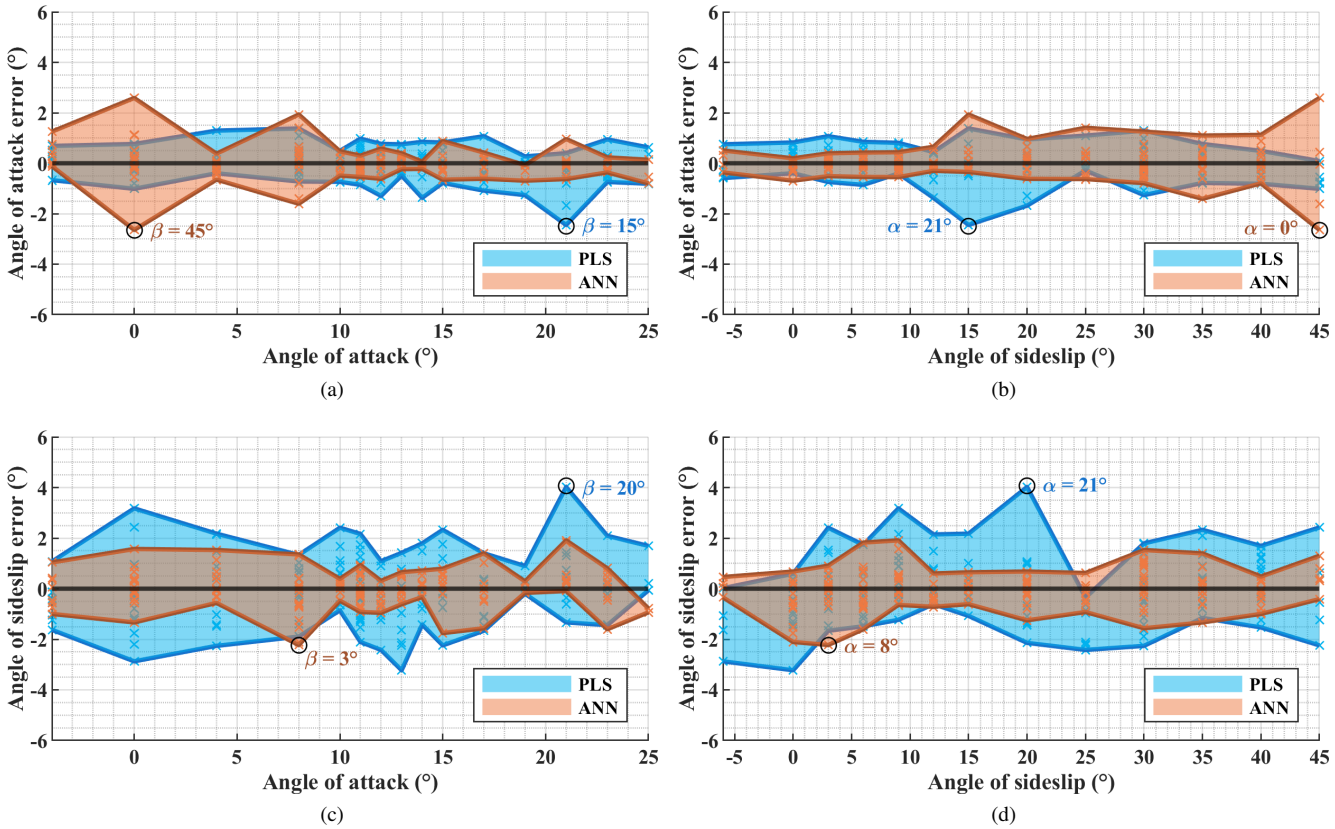

Fig. 5: Estimator error distribution comparisons: **(a)** α estimation errors distributed across α, **(b)** α estimation errors distributed across β, **(c)** β estimation errors distributed across α, and **(d)** β estimation errors distributed across β. The shaded areas signify the range in estimation errors for the testing dataset, while the markers show the individual errors for each combination of angles tested. The annotations correspond to the angle combinations with the largest α and β estimation error magnitudes, coloured by estimator type.

Raines et al. in [2], where the angle at which non-linear pressure characteristics were observed (corresponding to the stall angle) varied with the span-wise location of the sensor. This characteristic was suggested to be useful as a stall early-warning system.

This work has also shown that the estimation of angle of sideslip is possible from pressure signals, even up to an extreme of $\alpha = 25°, \beta = 45°$. Furthermore, this estimation is possible to a reasonable degree of accuracy even with a linear estimator. This is a significant result that unlocks the potential of a 6 degree-of-freedom pressure-based "flight-by-feel" control system. Computationally cheap estimators, such as PLS-based regression, are key for allowing the real-time estimation required for a control system, especially on power and weight limited flight hardware.

There is also likely scope for improvement to the accuracy of estimation. Li et al. [21] achieved more accurate β estimation (exclusively for $\beta < 10°$) using a non-linear iterative robust regression model; they achieved a mean absolute error in β estimation of just 0.25°, compared to a mean absolute error of 0.53° achieved by the ANN estimator for the same range in this work. By contrast, their α estimation error agreed well with the present study, differing by less than 0.03°. The ANN estimator employed by Araujo-Estrada & Windsor in [20], however, was more accurate, with an overall α estimation RMSE of just 0.15° (over a range of $-15° \leq \alpha \leq 20°$) compared to the present study's 0.54°. The higher RMSE found here was largely due to the under-performance of the ANN estimator at low angles of attack, visible in Fig. 5a.

The relative under-performance of the ANN at α estimation in the $-6° \leq \alpha \leq 8°$ region (RMSE $= 0.82°$) is noteworthy, as this pre-stall region generally results in simple linear pressure variation with α. The under-performance here could be a sign of one of the weaknesses of the ANN estimation approach - its requirement for a large observation dataset. The region where the ANN performed most poorly is the sparsest region of the test matrix (see Fig. 3). It is possible that the ANN did not have sufficient granularity in this region to completely capture the relationship between the pressure signals and angle of attack, especially when this relationship was complicated by a high angle of sideslip, as annotated in Fig. 5a; the largest α estimation error was produced at the maximum tested β.

The annotations in Fig. 5 show that the largest estimation errors for each angle generally occurred when the other

angle was at or near its maximum value. This highlights the complex aerodynamic effects occurring at high β (such as fuselage interaction effects) and at post-stall α (stall effects). It is possible these respective effects interfere with the pressure signals in a way that complicates their relationship to angle changes, reducing the accuracy of estimation, especially for an estimator with limited training data. The ANN's β estimation error was also slightly higher in the $-6^\circ \leq \alpha \leq 8^\circ$ region than at higher values of α, supporting the theory that lack of training data may have influenced the ANN's estimation performance. In contrast, the ANN estimator employed in [20] had very good performance at low angles, but also had access to a much larger training dataset.

Additionally, the loss function used to train the ANN was the mean-squared-error between the training dataset and the associated predictions (see Section IV-B); it is possible that, due to the higher test-point density in the stall/post-stall range, the loss function unintentionally weighted the ANN towards better representation in this range to the detriment of the linear region. This is a limitation that could be further explored by trialling different training techniques.

Although influenced by this apparent lack of data for the $\alpha < 10^\circ$ range, it is also noteworthy that the overall RMSE for α estimation was very similar between the linear and non-linear estimator. This is contradictory to the result found in [20], in which the non-linear estimator substantially outperformed the linear estimator in the post-stall region. This may be partly explained by the gentle stall experienced by the chosen wing at these Reynolds numbers; as seen in Fig. 4a, no sudden losses of lift were experienced at stall. It is likely that a sharper stall would result in more complex correlations of the pressure signals in response to α, which could reduce the effectiveness of a PLS-based estimator: the work in [20] included dynamic experiments at higher Reynolds numbers, which would be more likely to cause sharper stalling effects. Investigation of distributed pressure sensing arrays on a wing section with harsher stalling characteristics could confirm this.

Overall, this work has extended the distributed pressure sensing state of the art by demonstrating that good predictions of both α and β are possible, even well after stall. This unlocks the possibility of a robust model-based controller informed by pressure sensing signals. The results show that a linear estimation approach is suitable for use in control for both α and β, though β estimation shows greater improvements from the use of a non-linear estimator than α. The results have also shown the value of a pressure sensing array across multiple span-wise locations, as a tool to encode a large amount of flow information in both longitudinal and lateral directions.

Future work could take three avenues. Firstly, the existing dataset could be investigated as a means to predict not only the aerodynamic states but also the associated aerodynamic loads, expanding the work in [20] to include lateral loads. Secondly, the importance of specific sensor placements, especially in the span-wise direction, could be studied; it has been seen from these results, for example, that the inboard sensors are more sensitive to changes in β than the outboard ones. Lastly, the control surfaces on the distributed sensing UAV could be deployed in wind tunnel tests to assess their impact on the estimation of aerodynamic states and loads. This is an important aspect that must be understood before a distributed sensing-based flight controller can be built.

VI. CONCLUSIONS

Wind tunnel tests were carried out on a bio-inspired distributed sensing UAV at high angles of attack and sideslip. Aerodynamic loads and distributed pressure sensing measurements from four span-wise sensor strips were acquired for each experimental condition. The high spatial resolution of the pressure data captured significant information about the aerodynamic state of the vehicle, demonstrating for the first time accurate estimation of both longitudinal and lateral-directional aerodynamic angles even in the complex post-stall flow regime, up to $\alpha = 25^\circ$ and $\beta = 45^\circ$. The linear PLS-based estimator's performance was comparably strong to the ANN estimator for angle of attack estimation, possibly due to the gentle stalls that are characteristic of the wing section. However, the ANN performed markedly better than the PLS-based estimator for angle of sideslip predictions, suggesting non-linear behaviour as angle of sideslip increases. This work has demonstrated that pressure-based distributed sensing provides accurate estimates of both longitudinal and lateral-directional aerodynamic states. These could inform a robust "flight-by-feel" controller, unlocking greater manoeuvrability and gust rejection for fixed-wing UAVs. This is particularly desirable for applications that require flight through cluttered urban areas, such as last-mile cargo delivery.

ACKNOWLEDGMENT

The authors would like to thank Dr David Marshall and Dr Renan Soares from the University of Southampton's R.J. Mitchell wind tunnel, whose support in operating the tunnel was invaluable. The authors would also like to thank Sanuja Jayatilake and Munmeet Bahra for their parts in modifying and assembling the distributed sensing UAV.

This work was supported by the Engineering and Physical Sciences Research Council, under a Doctoral Training Partnership (DTP) Scholarship. The authors would like to thank the School of Engineering at the University of Southampton for providing a PhD studentship to Sourish Mukherjee.

REFERENCES

[1] S. A. H. Mohsan, N. Q. H. Othman, Y. Li, M. H. Alsharif, and M. A. Khan, "Unmanned aerial vehicles (UAVs): Practical aspects, applications, open challenges, security issues, and future trends," *Intelligent Service Robotics*, Jan. 2023.

[2] M. M. Groves-Raines, S. A. Araujo-Estrada, A. Mohamed, S. Watkins, and S. P. Windsor, "Wind tunnel testing of an avian-inspired morphing wing with distributed pressure sensing," in *2022 International Conference on Unmanned Aircraft Systems (ICUAS)*, Jun. 2022, pp. 290–299.

[3] S. Watkins, J. Milbank, B. J. Loxton, and W. H. Melbourne, "Atmospheric Winds and Their Implications for Microair Vehicles," *AIAA Journal*, vol. 44, no. 11, pp. 2591–2600, Nov. 2006.

[4] A. Mohamed, K. Massey, S. Watkins, and R. Clothier, "The attitude control of fixed-wing MAVS in turbulent environments," *Progress in Aerospace Sciences*, vol. 66, pp. 37–48, Apr. 2014.

[5] A. Mohamed, R. Clothier, S. Watkins, R. Sabatini, and M. Abdulrahim, "Fixed-wing MAV attitude stability in atmospheric turbulence, part 1: Suitability of conventional sensors," *Progress in Aerospace Sciences*, vol. 70, pp. 69–82, Oct. 2014.

[6] P. Vörsmann, C. Kaschwich, T. Krüger, P. Schnetter, and C.-S. Wilkens, "MEMS based integrated navigation systems for adaptive flight control of unmanned aircraft-state of the art and future developments," *Gyroscopy and Navigation*, vol. 3, no. 4, pp. 235–244, 2012.

[7] J. Perry, A. Mohamed, B. Johnson, and R. Lind, "Estimating Angle of Attack and Sideslip Under High Dynamics on Small UAVs," in *Proceedings of the 21st International Technical Meeting of the Satellite Division of The Institute of Navigation*, 2008, pp. 1165–1173.

[8] J. M. Levin, M. Nahon, and A. A. Paranjape, "Aggressive Turn-Around Manoeuvres with an Agile Fixed-Wing UAV," *IFAC-PapersOnLine*, vol. 49, no. 17, pp. 242–247, 2016.

[9] M. Basescu, A. Polevoy, B. Yeh, L. Scheuer, E. Sutton, and J. Moore, "Agile Fixed-Wing UAVs for Urban Swarm Operations," *IEEE Transactions on Field Robotics*, vol. 1, pp. 394–423, 2024.

[10] D. L. Altshuler, J. W. Bahlman, R. Dakin, A. H. Gaede, B. Goller, D. Lentink, P. S. Segre, and D. A. Skandalis, "The biophysics of bird flight: Functional relationships integrate aerodynamics, morphology, kinematics, muscles, and sensors," *Canadian Journal of Zoology*, vol. 93, no. 12, pp. 961–975, Dec. 2015.

[11] R. Zbikowski, "Sensor-rich feedback control: A new paradigm for flight control inspired by insect agility," *IEEE Instrumentation & Measurement Magazine*, vol. 7, no. 3, pp. 19–26, Sep. 2004.

[12] S. J. Sterbing-D'Angelo, M. Chadha, K. L. Marshall, and C. F. Moss, "Functional role of airflow-sensing hairs on the bat wing," *Journal of Neurophysiology*, vol. 117, no. 2, pp. 705–712, Feb. 2017.

[13] W. Hörster, "Vibrational sensitivity of the wing of the pigeon (Columba livia) — a study using heart rate conditioning," *Journal of Comparative Physiology A*, vol. 167, no. 4, pp. 545–549, Sep. 1990.

[14] R. E. Brown and M. R. Fedde, "Airflow Sensors in the Avian Wing," *Journal of Experimental Biology*, vol. 179, no. 1, pp. 13–30, Jun. 1993.

[15] A. C. Hollenbeck, R. Grandhi, J. H. Hansen, and A. M. Pankonien, "Bioinspired Artificial Hair Sensors for Flight-by-Feel of Unmanned Aerial Vehicles: A Review," *AIAA Journal*, vol. 61, no. 12, pp. 5206–5231, 2023.

[16] S. A. Araujo-Estrada, F. Salama, C. M. Greatwood, K. T. Wood, T. S. Richardson, and S. P. Windsor, "Bio-inspired Distributed Strain and Airflow Sensing for Small Unmanned Air Vehicle Flight Control," in *AIAA Guidance, Navigation, and Control Conference*, ser. AIAA SciTech Forum, Jan. 2017.

[17] A. Mohamed, S. Watkins, R. Clothier, M. Abdulrahim, K. Massey, and R. Sabatini, "Fixed-wing MAV attitude stability in atmospheric turbulence—Part 2: Investigating biologically-inspired sensors," *Progress in Aerospace Sciences*, vol. 71, pp. 1–13, Nov. 2014.

[18] K. T. Wood, S. Araujo-Estrada, T. Richardson, and S. Windsor, "Distributed Pressure Sensing–Based Flight Control for Small Fixed-Wing Unmanned Aerial Systems," *Journal of Aircraft*, vol. 56, no. 5, pp. 1951–1960, Sep. 2019.

[19] K. T. Magar, G. W. Reich, C. Kondash, K. Slinker, A. M. Pankonien, J. W. Baur, and B. Smyers, "Aerodynamic parameters from distributed heterogeneous CNT hair sensors with a feedforward neural network," *Bioinspiration & Biomimetics*, vol. 11, no. 6, Nov. 2016.

[20] S. A. Araujo-Estrada and S. P. Windsor, "Aerodynamic State and Loads Estimation Using Bioinspired Distributed Sensing," *Journal of Aircraft*, vol. 58, no. 4, pp. 704–716, Jul. 2021.

[21] N. Li, W. Zou, Y. Zhu, B. Wang, S. Bu, and H. Shen, "A Compact Embedded Flight Parameter Detection System for Small Soaring UAVs," *IEEE/ASME Transactions on Mechatronics*, vol. 29, no. 1, pp. 52–63, Feb. 2024.

[22] D. Yeo, E. M. Atkins, L. P. Bernal, and W. Shyy, "Experimental Validation of an Aerodynamic Sensing Scheme for Post-Stall Aerodynamic Moment Characterization," in *AIAA Atmospheric Flight Mechanics (AFM) Conference*, Aug. 2013.

[23] S. A. Araujo-Estrada and S. P. Windsor, "Artificial Neural Network-Based Flight Control Using Distributed Sensors on Fixed-Wing Unmanned Aerial Vehicles," in *AIAA Scitech 2020 Forum*, Orlando, FL, Jan. 2020.

[24] K. P. T. Haughn, C. Harvey, and D. J. Inman, "Deep learning reduces sensor requirements for gust rejection on a small uncrewed aerial vehicle morphing wing," *Communications Engineering*, vol. 3, no. 1, pp. 1–11, Mar. 2024.

[25] A. Guerra-Langan, S. Araujo Estrada, and S. Windsor, "Reinforcement Learning to Control Lift Coefficient Using Distributed Sensors on a Wind Tunnel Model," in *AIAA SCITECH 2022 Forum*, San Diego, CA & Virtual, Jan. 2022.

[26] C. Leys, C. Ley, O. Klein, P. Bernard, and L. Licata, "Detecting outliers: Do not use standard deviation around the mean, use absolute deviation around the median," *Journal of Experimental Social Psychology*, vol. 49, no. 4, pp. 764–766, Jul. 2013.

[27] Z. Didyk and V. Apostolyuk, "Whole angle approximations of aerodynamic coefficients," in *2012 2nd International Conference "Methods and Systems of Navigation and Motion Control" (MSNMC)*, Kiev, Ukraine, Oct. 2012, pp. 119–121.

[28] H. Abdi and L. J. Williams, "Partial Least Squares Methods: Partial Least Squares Correlation and Partial Least Square Regression," in *Computational Toxicology*, Totowa, NJ, 2013, vol. 930, pp. 549–579.

[29] K. Hornik, M. Stinchcombe, and H. White, "Multilayer feedforward networks are universal approximators," *Neural Networks*, vol. 2, no. 5, pp. 359–366, Jan. 1989.

[30] D. C. Liu and J. Nocedal, "On the limited memory BFGS method for large scale optimization," *Mathematical Programming*, vol. 45, no. 1, pp. 503–528, Aug. 1989.

[31] D. Chen, F. Kaiser, J. Hu, D. E. Rival, K. Fukami, and K. Taira, "Sparse Pressure-Based Machine Learning Approach for Aerodynamic Loads Estimation During Gust Encounters," vol. 62, no. 1, pp. 275–290.

APPENDIX

Measured loads are given by:

$$F_m = F_{Aero} + F_{Inertial} + F_{Strut} \tag{A.1}$$

Note that we are only interested in F_{Aero}. To remove effects from the other two components, we carried out the following calibration tests:

1) $F_{Inertial}$ was removed prior to each data collection by balance calibration with the attached UAV.
2) To identify F_{Strut}, we measured the forces acting only on the struts throughout the range of the α and β for the three wind speeds. The forces were then characterised using (A.4).

Similarly, the measured moments are given by:

$$M_m = M_{Aero} + M_{Inertial} + M_{Strut} + M_{Virtual} \tag{A.2}$$

The following procedure was carried out to extract the M_{Aero}:

1) $M_{Inertial}$ was identified by measuring the moments for varying α and β with no wind. (A.4) was applied to characterise the data.
2) M_{Strut} removal followed a similar procedure as F_{Strut}, where the moments were measured alongside the forces.
3) $M_{Virtual}$ refers to lift and drag contributions to the moments due to their measurement in the wind tunnel reference frame. This was characterised as follows:

$$M_{virtual} = \frac{C_l \cdot x - C_d \cdot y}{c} \tag{A.3}$$

where x and y are sinusoidal functions of α, and refer to the vertical and horizontal distance from the quarter chord to the wind tunnel reference point.

Generic equation used for plane approximation during correction:

$$\hat{Y} = A \cdot sin(\omega_1 \alpha + p_1) + B \cdot sin(\omega_2 \beta + p_2) \tag{A.4}$$

where ω, p, A and B are regression-estimated coefficients.